Environ. Sci. Technol. **2006**, *40,* 2254−2261

Low Frequency Electrical Properties of Corroded Iron Barrier Cores

YUXIN WU,*,† LEE D SLATER,† AND
NIC KORTE‡

Department of Earth and Environmental Sciences, Rutgers University, Newark, New Jersey 07102, 1946 Clover Court, Grand Junction, Colorado 81506

We investigated the electrical signatures of iron corrosion and mineral precipitation in angle cores from an Fe^0 barrier installation in operation for eight years. The real and imaginary parts of the complex electrical conductivity measured between 0.1 and 1000 Hz were 2−10 times higher (varying between cores) in the reacted zone at the upgradient edge of the barrier relative to less altered locations inside the barrier. Scanning electron microscopy identified iron surface alteration with the thickest corrosion rinds closest to the upgradient soil/iron interface. Surface area of iron minerals was also greatest at the upgradient interface, gradually decreasing into the cores. X-ray diffractometry identified precipitation of iron oxide/hydroxide, carbonate minerals, iron sulfide, as well as green rusts, with mineral complexity decreasing away from the interface. The electrical measurements correlate very well with the solid-phase analyses, and they verify that electrical methods could be used to assess or monitor iron corrosion and mineral precipitation occurring in Fe^0 barriers.

Introduction

Permeable reactive barriers (PRBs) composed of granular zerovalent iron (Fe^0) are an established technology for groundwater remediation (*1*−*7*). Iron corrosion and mineral precipitation due to reactions between Fe^0 and groundwater constituents are widely recognized as the primary causes of Fe^0 barrier performance reduction (*8*−*15*). Corrosion and precipitation may result in formation of iron minerals that are less reactive with groundwater contaminants (*8*, *16*, *17*) and may also clog pore spaces (8, 10), thus reducing hydraulic efficiency (*3*, *8*, *18*).

Corrosion and precipitation is typically investigated by aqueous geochemical or solid phase analysis. Electrical methods can be used to indirectly assess iron corrosion and mineral precipitation processes. Tafel scan and electrochemical impedance spectroscopy (EIS) analysis of iron has identified geochemical controls on Fe^0 redox reactions (*19*−*21*). A recent study illustrated the sensitivity of four electrode electrical measurements (essentially an upscaled version of an EIS measurement) to corrosion and precipitation processes occurring in columns of granular Fe^0 as a result of invasion with simple electrolytes (*22*). This work illustrated the possibility of noninvasively monitoring precipitation in PRBs using electrical geophysical methods. Monitoring could be achieved by inserting electrode strings in the barrier during construction and recording the electrical changes as a function of time. This would conceivably reduce monitoring costs by eliminating the need for coring and solid-phase analysis or installation of monitoring wells for geochemical analysis

The electrical properties of a soil can be stated in terms of a measured frequency (ω) dependent complex conductivity $\sigma^*(\omega)$,

$$\sigma^*(\omega) = \sigma'(\omega) + i\sigma''(\omega) \qquad (1)$$

where σ' is the measured real part of $\sigma^*(\omega)$, being the conduction component, and σ'' is the measured imaginary part of $\sigma^*(\omega)$, being the polarization component ($i = \sqrt{-1}$). Charge transfer in granular Fe^0 columns can be attributed to three mechanisms (*22*). First, σ_{el} represents the conductivity of the interconnected, fluid-filled pore space (a real term); second, σ^*_{int} is a complex term describing conduction and polarization at the iron mineral/electrolyte interfaces; third, σ_{elc} accounts for electronic conduction (a real term) through the iron minerals. The σ_{el} is linearly dependent on the conductivity (σ_w) of the electrolyte saturating the Fe^0 column. The σ^*_{int} incorporates both conduction along the electrical double layer (EDL) and polarization occurring at the electrolyte/iron mineral interface. It includes a diffusive mechanism (σ^*_{mdiff}) that linearly increases with the metallic surface area (*23*, *24*) and an electrochemical mechanism (σ^*_{melc}) associated with redox active ions that permit electrical current to bridge between electrolytic conduction (σ_{el}) in the pore space and electronic conduction (σ_{elc}) in iron minerals (*23*). The measured σ' therefore depends on σ_{el}, σ_{elc}, and σ^*_{int} whereas σ'' is only dependent on σ^*_{int} (i.e., it exclusively relates to the interfacial properties of the iron minerals).

Measurements on Fe^0-sand mixtures show that the polarization (σ'') is linearly related to the specific surface area of the iron minerals in an Fe^0 column (*24*). Furthermore, Wu et al. (*22*) observed an increase in σ'' following corrosion and precipitation induced in Fe^0 columns that they primarily attributed to the increase in S_s of the iron minerals due to surface alteration. EIS measurements have demonstrated that electrical conduction (σ') increases after iron corrosion and mineral precipitation due to increased metallic mineral/electrolyte surface area combined with enhanced electronic conduction in electroactive precipitants, primarily magnetite (*21*). Wu et al. (*22*) similarly observed an increase in σ' of reacted Fe^0 columns that occurred coincident with precipitation of iron corrosion products including magnetite.

In this paper we describe low-frequency electrical measurements on angle cores recovered from an iron barrier that has been in operation for eight years. Surface morphology, mineral phase analysis, and core material elemental analysis were performed to evaluate the sensitivity of electrical measurements on iron corrosion and mineral precipitation along the cores. These measurements were also compared with barrier aqueous geochemistry evaluated with a network of boreholes at the site. The results show that electrical measurements reflect the amount of corrosion and precipitation occurring in an operative Fe^0 PRB. Significantly, the electrical signatures on these cores are much greater than those recorded in previous synthetic studies on Fe^0 columns (*22*). These findings conclusively demonstrate the applicability of low-frequency electrical methods for long-term monitoring of iron barriers.

Materials and Methods

Site Description. The PRB under study was installed in April 1998 at the Kansas City Plant (KCP) operated by the U.S.

---

* Corresponding author phone: (973) 596-5863; e-mail: yuxinwu@pegasus.rutgers.edu.

† Rutgers University.

‡ Grand Junction, Colorado.

10.1021/es0520868 CCC: $33.50

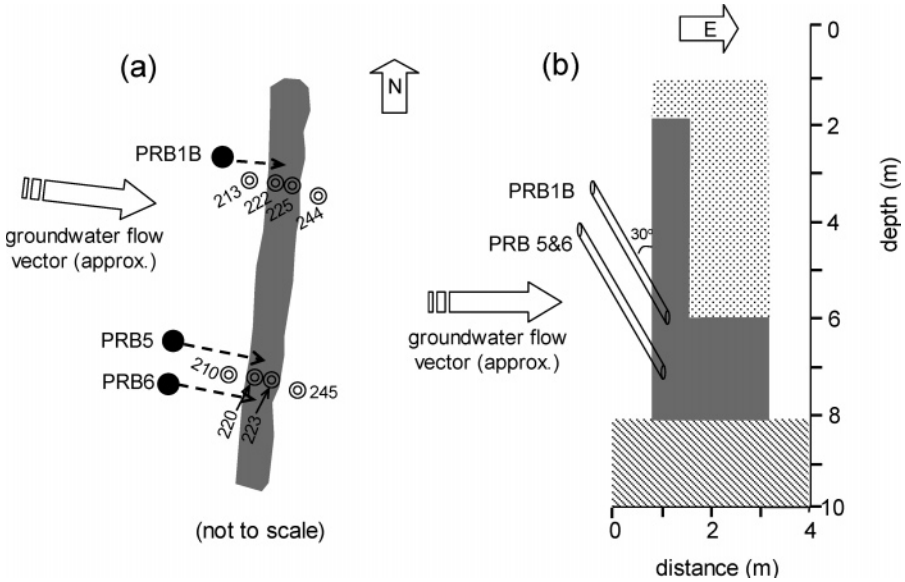

FIGURE 1. (a) Plan view and (b) cross section of KCP Fe^0 barrier showing the outline of the barrier (Fe^0 (dark gray)), basic geology (sand (light gray), shale (hatched)), position of groundwater monitoring wells (◎) and cores (●).

Department of Energy (*25*). The barrier was designed to remediate 1, 2-dichloroethlene (1, 2-DCE) and chloroethene in contaminated groundwater migrating from the facility. Figure 1 (a, b) gives a plan and cross sectional view of the site. The PRB was constructed as a continuous 40 m (130 ft) long, 1.8 m (6 ft) wide trench. Alluvial sediments underlie the site, primarily silty clay overlying basal gravel. These alluvial sediments are underlain by bedrock shale. The PRB was constructed by filling the first 1.8 m (6 ft) of the trench with 100% iron such that the base of this section was in contact with bedrock. The remainder of the trench was then filled with 0.6 m (2 ft) of iron and 1.2 m (4 ft) of sand (Figure 1b). The thicker lower unit was designed to compensate for higher flow-through velocities associated with hydraulically conductive basal gravel resting on bedrock (Figure 1b).

The performance of the KCP−PRB has been adversely affected by alteration to groundwater flow resulting from the PRB structure itself (*25*). Hydraulic heads measured at the site show that flow is bypassing the southern end of the barrier. Geochemical measurements show incomplete reduction of organic compounds in monitoring wells on the outflow side of the barrier toward its southern end (*25*).

Material Aquisition. Three angle cores were recovered by driving a geoprobe containing plastic sleeves into the up gradient interface of the barrier at 30°off normal. Figure 1 shows the coring configuration. Core PRB1B penetrated the soil/iron interface at a depth of approximately 5.6 m and went into the barrier for approximately 30 cm; PRB5 and PRB6 penetrated the interface at about 7 m and went into the barrier about 22 cm. Immediately following extraction, natural soil was removed and cores were bathed in Argon to limit air oxidation and then sealed with plastic end caps. Visual observation showed that cores were generally black throughout with material closest to the upgradient soil/iron interface seemingly cemented and of finer particle size. A section of sand was encountered in the middle section of core PRB1B (Figure S1, Supporting Information).

Electrical Measurements. Figure S1 illustrates the measurement setup. Cores comprised the upgradient soil/iron interface, the cemented and finer material representing reacted iron on the upgradient edge of the barrier as well as less reacted iron deeper within the barrier. A gradual change from reacted to less reacted iron was observed and no distinct interface identified. SEM images (described later) suggest that the transition to pure unreacted Fe^0 was captured in PRB5 but it was not fully captured in PRB1B and PRB6.

Core holders were modified in an anaerobic chamber to permit electrical measurements. A stainless steel mesh was housed within the cap for current injection. Measuring (potential) electrode ports were installed at 3 cm intervals along the cores with the first port (port 1) just inside the Fe^0 at the upgradient soil/iron interface. The total number of ports varied according to the length of each core. Core PRB1B had eight ports, core PRB5 had six ports, and core PRB6 had five ports. Ag−AgCl potential electrodes were utilized for electrical measurements, and they were electrically coupled to the cores by inserting them into a saturated (with KCP water) port on the immediate edge of the sample in electrolytic contact with the Fe^0 core. This permitted accurate recording of the electric field within the column while avoiding polarization on the electrode that can result when potential electrodes are placed immediately within the sample and in the current flow path (*26*). Cores were resaturated with deoxygenated KCP groundwater (fluid conductivity (σ_w) = 0.073 ± 0.004 S/m) prior to electrical measurements. Electrical measurements were made between each pair of adjacent ports to acquire a sequence of electrical signatures from the soil/iron interface into the barrier.

The phase shift (ϕ) and conductivity magnitude ($|\sigma|$) for each section were recorded relative to a reference resistor (Figure S1) for forty frequencies spaced at equal logarithmic intervals from 0.1 to 1000 Hz. The real and imaginary parts of the complex conductivity were determined from the following equations:

$$\sigma'' = |\sigma| \times \sin\phi \qquad (2)$$

$$\sigma' = |\sigma| \times \cos\phi \qquad (3)$$

Electrical Data Modeling. Physically based models to describe $\sigma^*(\omega)$ of soils are lacking, and macroscopic representations, such as the Cole−Cole model (*27*), are typically adopted (see, for review, ref *28*). The dependence of complex conductivity with frequency was modeled as (*29*)

$$\sigma^* = \sigma_0\left[1 + m\left(\frac{(i\omega\tau)^c}{1 + (i\omega\tau)^c(1-m)}\right)\right] \qquad (4)$$

where σ_0 is the conductivity at DC frequency, τ is the mean relaxation time, c is a shape exponent (typically 0.1−0.6), and m is the chargeability (m = 1-σ_0/σ_∞, where σ_∞ is the conductivity at high frequency). The two model parameters of interest here are σ_0 and $m_n = m \times \sigma_0$, representing global measures of conduction and interfacial polarization respectively (*30*). We inverted electrical data using an algorithm based on a least-squares approach with Marquardt regularization (*31*).

Corrosion Assessment. Samples for solid-phase analysis were extracted from cores after completion of electrical measurements. Cross sectional scanning electron microscopy (SEM) imaging and S_s measurements were used to characterize changes in corrosion and precipitation along each core. One sample was acquired between each pair of adjacent ports and split into two subsamples for SEM imaging and S_s measurements. Samples were transported onto filter paper and gently washed with deoxygenated acetone/water solution (1:1 volume ratio) for approximately 2 min to eliminate residual solution. Samples were then left to dry in the anaerobic chamber for 4 h. Surface and cross-sectional SEM imaging was conducted for each sample to acquire a sequence of morphological changes along each core following the same procedure described in ref *22*.

The S_s of each sample was measured in triplicate with a five point Brunauer, Emmett, and Teller (BET) (*32*) method using a high-speed nitrogen sorption analyzer, model NOVA 3000 from Quantachrome instruments (Boynton Beach, Florida). The uncertainty of the measurements, based on the standard deviation of repeat measurements on a single sample, is less than 3%.

Mineral Phase Analysis. X-ray diffractometry (XRD), supported by SEM imaging was used for mineral phase identification. Ten grams of each sample were ground with an agate mortar and pestle to acquire fine grains. A Philips PW3040 powder X-ray diffractometer was employed following the same procedure described in ref *22*. Scans of $2\theta = 15-90°$ were acquired (scan rate of 0.02° per step). X′pert Highscore (Phillips Analytical B.V., Almelo, The Netherlands) was used for mineral phase identification.

Results and Discussion

Complex Conductivity. Figure 2 shows the changes of σ' and σ'' as a function of frequency for all three cores. The distance in the legend refers to the position of the midpoint of any two consecutive potential electrodes from the upgradient soil/iron interface (e.g., subsection between port 1 and 2 is represented as “1.5 cm”).

We excluded the following measurements from the plot in order to emphasize the differences in the electrical measurements that result exclusively from iron mineral alteration: (1) 1.5 cm in PRB6 as small portions of native soil were visually observed in the region 0−1 cm along this core (2) 7.5, 10.5, and 13.5 cm in PRB1B as a sand inclusion was encountered between 8 and 13 cm from the interface in this core (Figure S1). Figure 2 (a, c, and e) shows a continuous decrease of σ'' away from the soil/iron interface into each core. Figure 2 (b, d, and f) illustrates that a reduction in σ' also occurs with greater distance from the upgradient soil interface.

Figure 3 shows the variation of Cole−Cole model parameters m_n (Figure 3a) and σ_0 (Figure 3b) along the three cores. The modeling results are consistent with the behavior inferred from spectral data (Figure 2): m_n and σ_0 consistently decrease with distance from the upgradient soil interface. The model parameters are approximately 10 times higher at the interface in PRB5 relative to the last measurement at 13.5 cm on this core. For PRB1B and PRB6 the parameters are 2−4 times higher at the interface relative to the least reacted Fe^0 in each core (i.e., the last point on each of these cores). Figure 3c shows m_n and σ_0 for PRB1B replotted to include those locations where sand was sampled (7.5, 10.5, and 13.5 cm) in order to illustrate the dramatic decrease in m_n and σ_0 as a result of the sand inclusion.

Corrosion Level Analysis. Cross sectional SEM imaging indicates a decrease in the amount of surface corrosion with distance from the soil/iron interface into the barrier. Figure 4 shows selected SEM images for PRB1B and PRB5. Images for PRB6 are available in figure S3 of Supporting Information. The images suggest that the amount of surface corrosion differs between cores, being greatest in PRB1B.

For example, the image of PRB1B 1.5 cm (Figure 4a) reveals severe corrosion, with crumbling and cracking of iron particles. Further into the core at PRB1B 7.5 cm (Figure 4b), iron particles retain a thick corrosion rind, but crumbling and cracking are absent. PRB1B 16.5 cm (Figure 4c) shows only a thin and discontinuous corrosion rind suggesting minor corrosion; PRB1B 19.5 cm (image not presented for brevity) showed little evidence of corrosion rind.

Images of PRB5 1.5 cm (Figure 4d) also reveal a thick, continuous corrosion rind, although there is no visible crumbling or cracking of iron materials, suggesting less corrosion as compared with the same location in PRB1B; PRB5 7.5 cm (Figure 4e) shows a discontinuous, thin corrosion rind whereas PRB5 13.5 cm (Figure 4f) shows no corrosion rind. These results suggest that the corrosion front in PRB1B (collected at the northern end of the barrier) (≥16.5 cm) is considerably wider than in PRB5 (collected at the southern end of the barrier) (≤13.5 cm). PRB6 similarly showed a pattern of corrosion rind development, with samples close to the soil/iron interface showing more severe corrosion than samples far from it (Figure S3). The sample captured furthest from the soil/iron interface in this core (PRB6 10.5 cm) still showed a corrosion rind, particularly on smaller particles.

BET surface area measurements revealed a continuous decrease of S_s (from 10.9 m^2/g to 4.9 m^2/g in PRB1B, from 6.3 m^2/g to 4.0 m^2/g in PRB5, and from 13.3 m^2/g to 4.5 m^2/g in PRB6) from the most reacted (closest to soil/iron interface) to the least reacted iron (furthest to soil/iron interface) (Table S1). The high S_s at the soil/iron interface is consistent with surface complexity and a high fraction of fine mineral precipitates resulting from severe iron corrosion and mineral precipitation. Among the three cores, PRB1B had the largest S_s at most locations, indicating the most severe corrosion.

Mineral Precipitation Analysis. XRD scans and SEM equipped with energy-dispersive X-ray spectroscopy (EDX) provided qualitative information on likely mineral phases; these included iron oxide/hydroxide, carbonate minerals, sulfide minerals, green rusts, and quartz. All three cores exhibit similar XRD characteristics with mineralogical complexity decreasing with distance from the soil/iron interface into the core. XRD scans for core PRB5 are presented in Figure 5, and scans for PRB1B (Figure S5) and PRB 6 (Figure S6) are available in the Supporting Information.

All cores show evidence of iron oxide/hydroxide mineral phases. Magnetite (Fe_3O_4) was identified as the dominant iron oxide in all cores consistent with the reductive environment within the barrier (pH = 9−10 and Eh = −120 − −210 mV, Table 1a). Geochemical modeling with PHREEQC confirmed that magnetite is the major iron oxide forming under this pH-Eh range. The black color of the cores supports widespread existence of magnetite.

Siderite ($FeCO_3$), calcite (α-$CaCO_3$), aragonite (β-$CaCO_3$), as well as magnesite ($MgCO_3$) were identified as major carbonate minerals (Figure 5, S5, and S6), calcite being the dominant phase. The crystalline structure of calcite was identified in SEM images (Figure S4b, Supporting Information). Aragonite and siderite were identified in all cores. Geochemical modeling with PHREEQC showed that iron carbonate and calcium carbonate are oversaturated in the

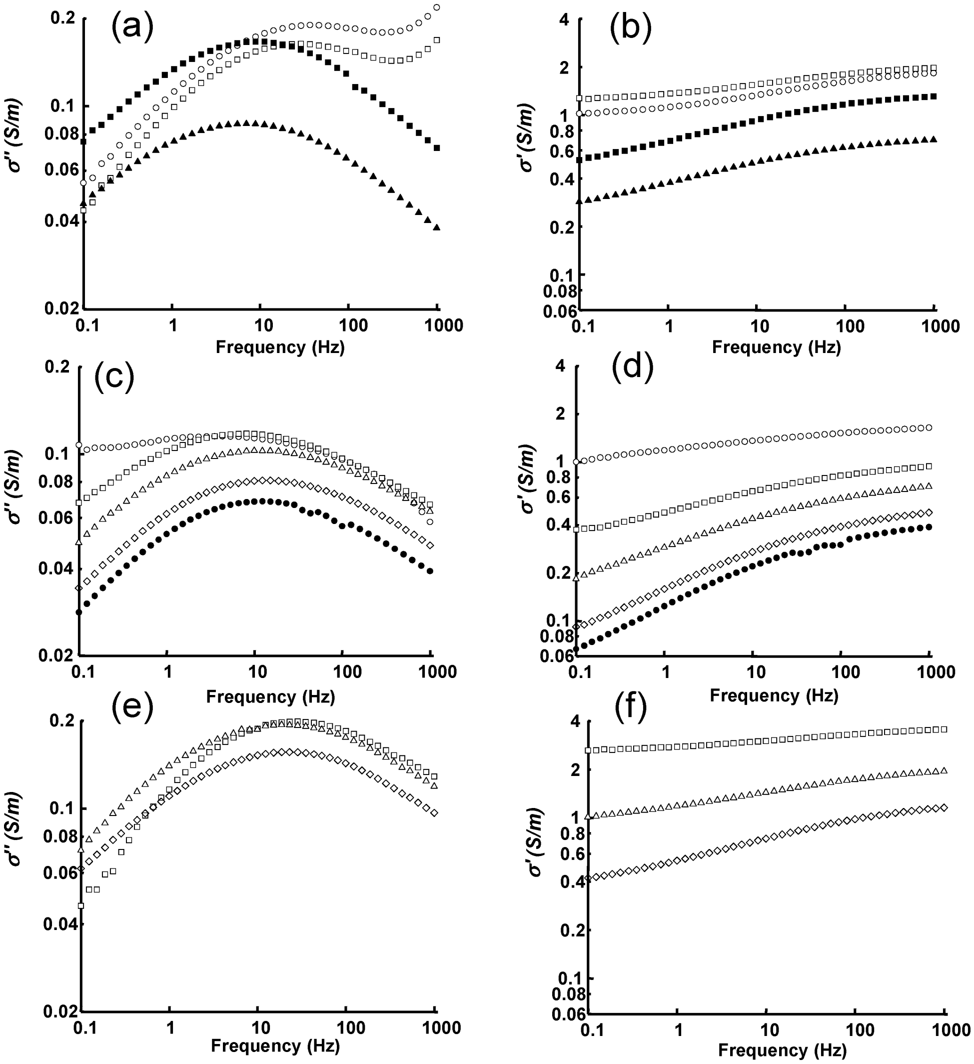

FIGURE 2. Spectral electrical data of three cores at different locations (1.5 (○), 4.5 (□), 7.5 (△), 10.5 (◇), 13.5 (●), 16.5 (■), and 19.5 (▲) cm): (a) σ'' of core PRB1B; (b) σ' of core PRB1B; (c) σ'' of core PRB5; (d) σ' of core PRB5; (e) σ'' of core PRB6; (f) σ' of core PRB6. Data are plotted on logarithmic scale. The three measurements from 7.5 to 13.5 cm for PRB1B and that from 1.5 cm for PRB6 are not plotted as they were not 100% PRB material (Figure S1).

barrier and can precipitate under the given geochemical conditions (Table 1a). Moreover, groundwater geochemical analysis (Table 1a) suggests significant removal of Ca, Fe, and Mg and reduced alkalinity in the barrier, providing evidence for iron/calcium/magnesium carbonate mineral precipitation. Core material elemental analysis (Table 1b) showed precipitation of Ca and Inorganic Carbon (IC) further supporting carbonate mineral precipitation. Note that concentrations of Ca and C were higher in PRB1B than in PRB5 and PRB6, indicating more intensive iron corrosion and mineral precipitation at the north end of the barrier.

Iron sulfides were also identified by XRD (Figure 5, S5 and S6). SEM/EDX revealed that Fe and S are major elements of elongated circular-shaped mineral aggregates (Figure S4c, Supporting Information), possibly being sulfate reducing bacteria covered by iron sulfide. Groundwater geochemical analysis (Table 1a) revealed a decrease of SO_4^{2-} from 10 to 25 mg/L outside of the barrier to below 2 mg/L within the barrier. Sulfur was also identified in core material elemental analysis at higher concentrations in PRB1B than in PRB5 and PRB6 (Table 1b) further suggesting greater reactivity toward the north of the barrier.

Green rusts (mineral phases of mixed Fe^{2+}/Fe^{3+} oxy (hydroxide) layers with anions (i.e., Cl^-, CO_3^{2-}, SO_4^{2-}) frequently incorporated into inner-layer spaces (*33*) were identified by XRD in all cores (Figure 5, S5 and S6) and a characteristic hexagonal platelet morphology observed with SEM surface imaging (Figure S4a, Supporting Information) (*33*, *34*). Quartz was identified in most of the samples, probably due to both Si impurities (about 2%) in peerless iron and partial incorporation of natural soil or sand into the barrier. Geochemical monitoring also revealed significant reduction of silica in the barrier (Table 1a).

Interpretation of Electrical Measurements. Our geochemical analyses indicate that the complex conductivity variation in these cores is directly related to Fe^0 corrosion and mineral precipitation. The gradual decrease in the real and imaginary parts of the complex conductivity and equivalent Cole–Cole model parameters with distance into the barrier coincides with the gradual decrease in surface morphological and mineralogical alteration due to corrosion and precipitation with distance from the upgradient soil/iron interface. The gradients of the m_n and σ_0 curves of PRB1B (Figure 3a and b) are less than those of PRB5 and PRB6, indicating a wider interface of corrosion at PRB1B. This is consistent with the cross sectional SEM imaging, which clearly shows that PRB1B exhibits a wider zone of corrosion and precipitation relative to the other cores. Furthermore, aqueous geochemistry

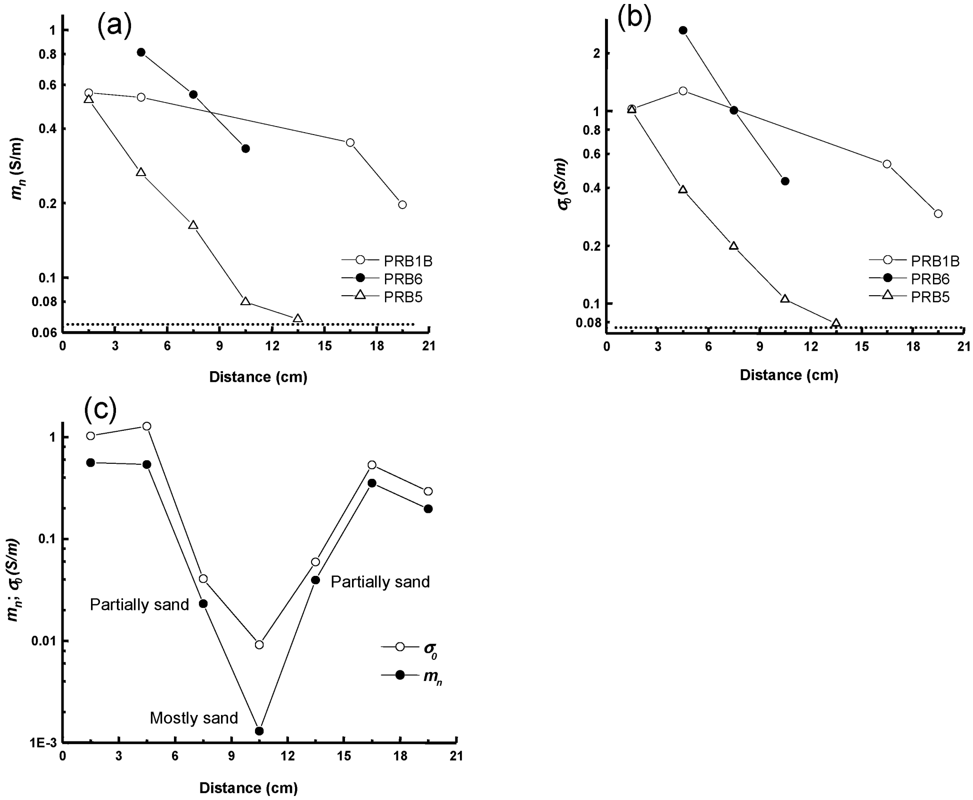

FIGURE 3. Cole−Cole model parameters m_n and σ_0 as a function of distance from the soil/iron interface for three cores (a) m_n (b) σ_0 ((PRB1B (○), PRB5 (△), PRB6 (●)).The dashed lines in (a) and (b) represent the values of unreacted iron. Each plot has a logarithmic *y*-axis and linear *x*-axis. (c) PRB1B replotted to include the samples affected by the sand encountered in this core from 8 to 13 cm (σ_0 (○), m_n (●)).

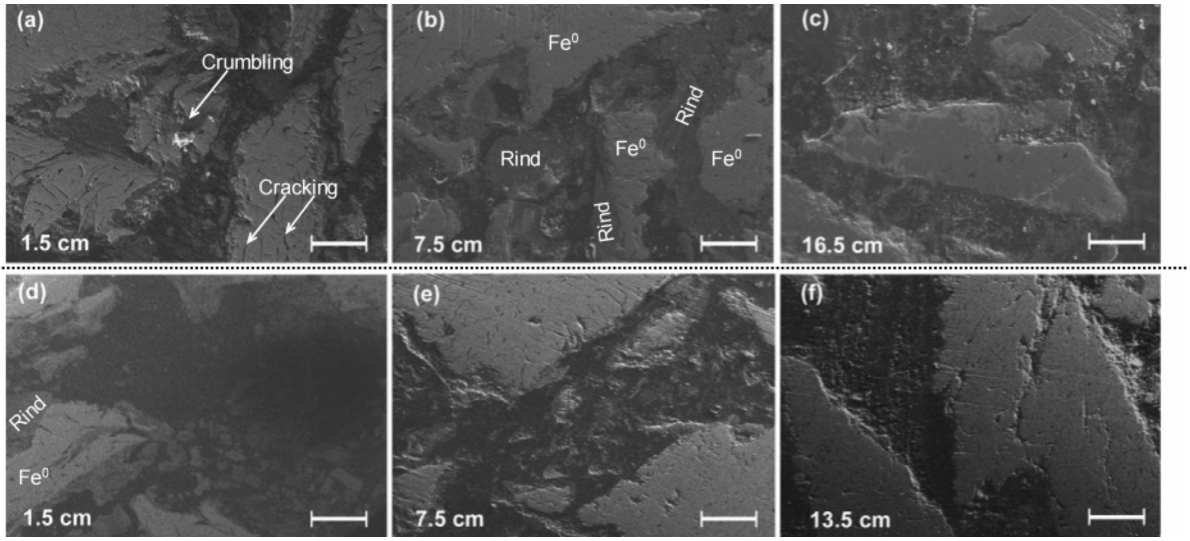

FIGURE 4. Cross sectional SEM image sequences of PRB1B and PRB5: (a) PRB1B 1.5 cm; (b) PRB1B 7.5 cm; (c) PRB1B 16.5 cm; (d) PRB5 1.5 cm; (e) PRB5 7.5 cm and (f) PRB5 13.5 cm. Bar: 200 μm.

suggests that preferential flow close to PRB1B results in greater precipitation of carbonates and sulfides at this end of the barrier.

Cole−Cole modeling of electrical measurements on unreacted peerless iron (obtained directly from the supplier) saturated with KCP groundwater resulted in values of m_n and σ_0 of 0.06 S/m and 0.07 S/m respectively (Figure 3). The respective values at 13.5 cm in PRB5 are $m_n = 0.068$ S/m and $\sigma_0 = 0.079$ S/m, suggesting that the sample obtained here is essentially unreacted Fe^0. The core for PRB5, therefore, probably captured the full interface of reacted/unreacted iron. However, m_n and σ_0 are much higher at 19.5 cm in PRB1B and 10.5 cm in PRB6, indicating some reacted iron at these locations and implying that the interface of reacted/unreacted iron in these cores was not fully captured. This conclusion is again well supported by SEM imaging. For example, the image at 10.5 cm for PRB6 exhibits a clear corrosion rind (Figure S3d), whereas the image at 13.5 cm in PRB5 shows little evidence of corrosion (Figure 4f).

We attribute the increased complex conductivity associated with increasing corrosion and precipitation to the combined effects of Fe^0 surface morphological change and mineralogical alteration, consistent with laboratory experiments (*22*). The increase of S_s due to iron corrosion and mineral precipitation increases the metal/electrolyte contact area and thus enhances interfacial polarization; it also

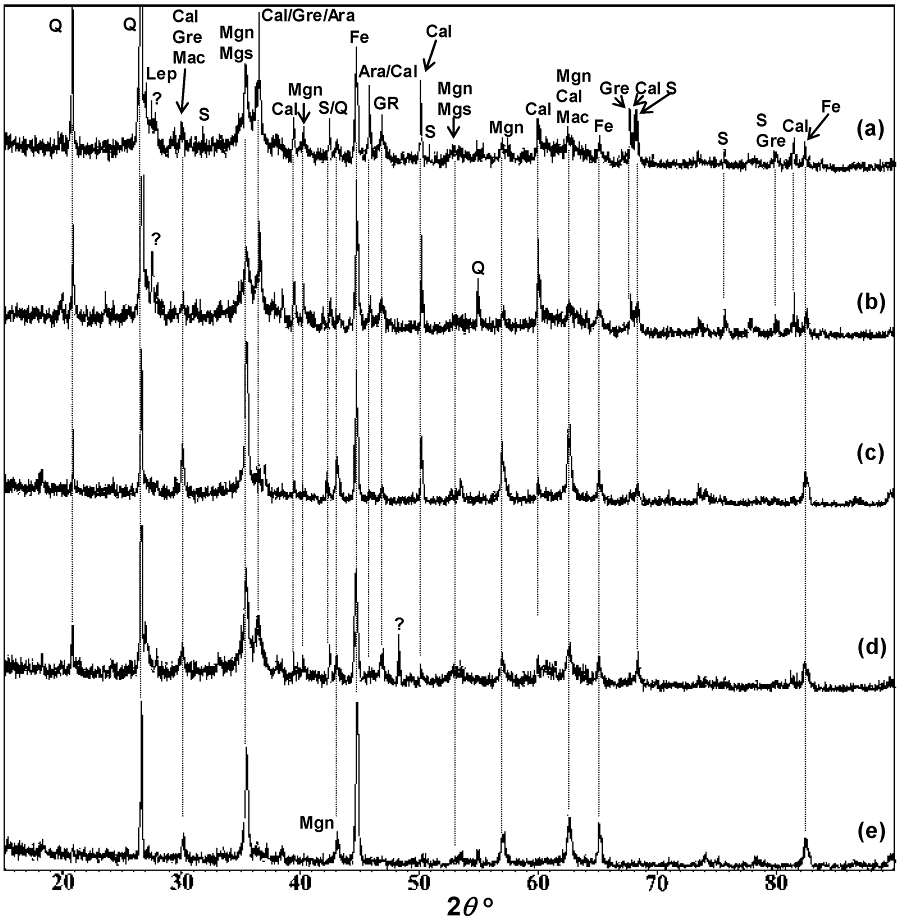

FIGURE 5. X-ray diffractograms of samples from PRB5 at locations: (a) 1.5 cm; (b) 4.5 cm; (c) 7.5 cm; (d) 10.5 cm; (e) 13.5 cm. (Mgh—maghemite, Mgn—magnetite, Cal—calcite, Ara—aragonite, S—siderite, Mgs—magnesite, Gre—greigite, Mac—mackinawite, Lep—lepidocrocite, GR—green rusts, Fe—Fe^0, Q-quartz).

TABLE 1. KCP Barrier Groundwater Geochemistry and Core Material Elemental Analysis

GroundWater Geochemistry Data[a]

	location	well#	pH	Eh	alkalinity	Ca	Mg	Mn	silica	Fe	SO_4
PRB1B	upgradient	213	6.6	−105.2	553	207	18.7	3.86	45.5	41.5	9.18
	in barrier	222	9.8	−170	49	13.9	0.07	0	1.69	0	0
		225	10	−213.6	47	5.64	0.23	0	2.88	0.053	1.9
	downgradient	244	9.3	−129.8	30	37.8	1.35	0.01	1.7	0.0525	85.8
PRB5&6	upgradient	210	6.8	−118	452	181	16.4	3.55	36.8	25	25.8
	in barrier	220	9	−182.9	34	36.2	1.89	0	0	0	0
		223	9.7	−119.9	36	31.8	2.76	0.07	0		0
	downgradient	245	7.2	−124.9	422	178	15.5	4.24	45.9	25.3	34.8

Core Material Elemental Analysis Data[b]

name	PRB1B							PRB5					PRB6			
	1.5	4.5	7.5	10.5	13.5	16.5	19.5	1.5	4.5	7.5	10.5	13.5	1.5	4.5	7.5	10.5
IC	367	269	373	634	11	168	245	25	110	128	228	252	128	17	116	60
Ca	119			1580	526			295	998	276	263	248				
S	49	59	161	81	77	63	31	1	50	40	56	68	39	38	54	24

[a] Unit: ppm for alkalinity and ion concentrations. [b] Unit: ppm.

increases conduction as there are more sites for redox-driven charge transfer across the metal/electrolyte interface. This is supported by EIS results showing that corrosion reduces the charge transfer resistance across the metallic mineral/electrolyte interface (*20*, *21*). Under the condition of minimally altered metallic mineral phase, a near-linear correlation between m_n and BET estimated S_s has been observed (*24*). However, significant mineral phase changes, as observed in these cores, prevent establishment of a simple quantitative relationship between m_n and BET estimated S_s (*22*).

Our results suggest that conduction increases more than polarization in response to mineralogical alteration and corrosion and the formation of secondary mineral phases in these cores. We attribute this to the nature of the mineralogical alteration of the iron surface. Nanoporous precipitates that still allow charge transfer between Fe^0 redox sites and electrolyte, as well as nonporous, electroactive precipitates, can both provide electron pathways between Fe^0 and electrolyte that enhance redox reactions and thus electronic conduction by facilitating charge transfer from the Fe^0 surface to oxidants in electrolyte (*20*). Magnetite, the dominant mineral phase in these cores, is particularly effective at facilitating such charge transfer (*35*), such that magnetite precipitation improves conduction in metallic minerals (*21*).

Research on iron corrosion has shown that minerals precipitate either as an iron surface coating, increasing surface complexity (hence, surface area), or as discrete mineral clusters, infilling pores that can reduce surface area under severe clogging (*8*, *9*, *17*). Only mild clogging by iron minerals close to the soil/iron interface was observed in cores during sample preparation. Research shows that major mineral phases contributing to porosity loss are $CaCO_3 > Fe_3O_4$ (*10*). Core material elemental analysis was used to estimate porosity loss due to $CaCO_3$ precipitation (Table 1b) applying the standard used in ref *34* that 3.2 mg of C per g of Fe could account for a void volume reduction of ~5%. A 3.2% porosity loss was calculated at the soil/iron interface, decreasing into the cores. This small porosity loss is consistent with our results in that conduction and polarization both increase as expected following precipitation of surface coatings and discrete fine particles.

Our previous results on synthetic laboratory Fe^0 columns revealed 23–35% increases of m_n and 25–45% increases of σ_0 resulting from short-term iron corrosion and mineral precipitation (*22*). The field cores exhibit much greater changes in electrical properties (Figure 3) between the most and least reacted zones. This is expected as the corrosion and precipitation observed after eight years of operation of the Kansas City Plant PRB is much greater than that generated in our synthetic studies (as apparent from SEM). Thus it is clear that geoelectrical measurements have adequate sensitivity to detect mineralogical alteration within field PRB installations. Furthermore, results for core PRB1B (Figure 3c, S1) demonstrate that electrical measurements are very sensitive to contamination of the Fe^0 by nonmetallic minerals (in this case sand) and could, therefore, be applied for detecting flaws in the construction and installation of a PRB.

The clear relationship between low frequency electrical measurements and degree of corrosion in cores from a field PRB has confirmed that low-frequency electrical methods could be used to noninvasively evaluate iron corrosion and mineral precipitation in field PRB installations. The four-electrode measurement used here is readily up-scalable to a downhole measurement or even to electrical imaging (over a narrower range of low frequencies) using electrodes placed around the edge of the barrier (*14*). Long-term monitoring of indicators of performance reduction in PRBs using geoelectrical tools applied in the field, therefore, appears possible and should be encouraged.

Acknowledgments

This research was supported by the Environmental Management Science Program (EMSP) of the Office of Science, U.S. Department of Energy, grant DE-FG07-02ER63506. Andreas Kemna (Institute of Chemistry and Dynamics of the Geosphere, Forschungszentrum Jülich) provided Cole–Cole relaxation modeling support. The support of Joe Baker (Honeywell FM&T) for site logistics and sampling, and from Rick Wilkin (U.S. Environmental Protection Agency) and Robert S. Kerr Laboratory, Ada, Oklahoma for core analysis, is gratefully acknowledged.

Supporting Information Available

Schematic of the cores and electrical measurement setup; cross sectional SEM images of samples from PRB6; Surface SEM imaging of selected precipitates; XRD scans for samples from PRB1B showing identified phases; XRD scans for samples from PRB6 showing identified phases. This material is available free of charge via the Internet at http://pubs.acs.org.

Literature Cited

(1) Gu, B.; Liang, L.; Dickey, M. J.; Yin, X.; Dai, S. Reductive precipitation of uranium(VI) by zero-valent iron. *Environ. Sci. Technol.* **1998**, *32*, 3366–3373.

(2) Su, C. M.; Puls, R. W. In situ remediation of arsenic in simulated groundwater using zerovalent iron: Laboratory column tests on combined effects of phosphate and silicate. *Environ. Sci. Technol.* **2003**, *37*, 2582–2587.

(3) Blowes, D. W.; Ptacek, C. J.; Benner, S. G.; McRae, C. W. T.; Bennett, T. A.; Puls, R. W. Treatment of inorganic contaminants using permeable reactive barriers. *J. Contam. Hydrol.* **2000**, *45*, 123–137.

(4) Morrison, S. J.; Metzler, D. R.; Carpenter, C. E. Uranium precipitation in a permeable reactive barrier by progressive irreversible dissolution of zerovalent iron. *Environ. Sci. Technol.* **2001**, *35*, 385–390.

(5) Cantrell, K. J.; Kaplan, D. I.; Wietsma, T. W. Zero-valent Iron for the in-situ remediation of selected metals in groundwater. *J. Hazard. Mater.* **1995**, *42*, 201–212.

(6) Gandhi, S.; Oh, B. T.; Schnoor, J. L.; Alvarez, P. J. J. Degradation of TCE, Cr(VI), sulfate, and nitrate mixtures by granular iron in flow-through columns under different microbial conditions. *Water Res.* **2002**, *36*, 1973–1982.

(7) Kreuzer, H. Treating metal-contaminated groundwater—Permeable reactive barrier cleans superfund site. *Pollut. Eng.* **2000**, *32*, 12–14.

(8) Liang, L. Y.; Korte, N.; Gu, B. H.; Puls, R.; Reeter, C. Geochemical and microbial reactions affecting the long-term performance of in situ ‘iron barriers’. *Adv. Environ. Res.* **2000**, *4*, 273–286.

(9) Liang, L. Y.; Sullivan, A. B.; West, O. R.; Moline, G. R.; Kamolpornwijit, W. Predicting the precipitation of mineral phases in permeable reactive barriers. *Environ. Eng. Sci.* **2003**, *20*, 635–653.

(10) Kamolpornwijit, W.; Liang, L.; West, O. R.; Moline, G. R.; Sullivan, A. B. Preferential flow path development and its influence on long-term PRB performance: column study. *J. Contam. Hydrol.* **2003**, *66*, 161–178.

(11) Wilkin, R. T.; Puls, R. W.; Sewell, G. W. Long-term performance of permeable reactive barriers using zero-valent iron: Geochemical and microbiological effects. *Ground Water* **2003**, *41*, 493–503.

(12) Odziemkowski, M. S.; Schuhmacher, T. T.; Gillham, R. W.; Reardon, E. J. Mechanism of oxide film formation on iron in simulating groundwater solutions: Raman spectroscopic studies. *Corros. Sci.* **1998**, *40*, 371–389.

(13) Benner, S. G.; Blowes, D. W.; Molson, J. W. H. Modeling preferential flow in reactive barriers: Implications for performance and design. *Ground Water* **2001**, *39*, 371–379.

(14) Slater, L.; Binley, A. Evaluation of permeable reactive barrier (PRB) integrity using electrical imaging methods. *Geophysics* **2003**, *68*, 911–921.

(15) Reardon, E. J. Anaerobic Corrosion of Granular Iron—Measurement and Interpretation of Hydrogen Evolution Rates. *Environ. Sci. Technol.* **1995**, *29*, 2936–2945.

(16) Farrell, J.; Kason, M.; Melitas, N.; Li, T. Investigation of the long-term performance of zero-valent iron for reductive dechlorination of trichloroethylene. *Environ. Sci. Technol.* **2000**, *34*, 514–521.

(17) Mackenzie, P. D.; Horney, D. P.; Sivavec, T. M. Mineral precipitation and porosity losses in granular iron columns. *J. Hazard. Mater.* **1999**, *68*, 1–17.

(18) Phillips, D. H.; Gu, B.; Watson, D. B.; Roh, Y.; Liang, L.; Lee, S. Y. Performance evaluation of a zerovalent iron reactive barrier: Mineralogical characteristics. *Environ. Sci. Technol.* **2000**, *34*, 4169–4176.

(19) Melitas, N.; Conklin, M.; Farrell, J. Electrochemical Study of Arsenate and Water Reduction on Iron Media Used for Arsenic Removal from Potable Water. *Environ. Sci. Technol.* **2002**, *36*, 3188–3173.

(20) Melitas, N.; Farrell, J. Understanding Chromate reaction kinetics with corroding iron media using Tafel analysis and electrochemical impedance spectroscopy. *Environ. Sci. Technol.* **2002**, *36*, 5476–5482.

(21) Mishra, D.; Farrell, J. Understanding nitrate reactions with zerovalent iron using tafel analysis and electrochemical impedance spectroscopy. *Environ. Sci. Technol.* **2005**, *39*, 645−650.
(22) Wu, Y.; Slater, L. D.; Korte, N. Effect of precipitation on low-frequency electrical properties of zero-valent iron columns. *Environ. Sci. Technol.* **2005**, *39*, 9197−9204.
(23) Wong, J. An electrochemical model of the induced-polarization phenomenon in disseminated sulfide ores. *Geophysics* **1979**, *44*, 1245−1265.
(24) Slater, L. D.; Choi, J.; Wu, Y. Electrical properties of iron-sand columns: Implications for induced polarization investigation and performance monitoring of iron-wall barriers. *Geophysics* **2005**, *70*, G87−G94.
(25) Laase, A.; Korte, N.; Baker, J.; Dieckmann, P.; Vogan, J.; Focht, R. In *2nd International Conference on Remediation;* Wickramanavake, G., Gavaskar, A., Chen, A., Eds.; Battelle Press: Columbus, Ohio, 2000; pp 417−424.
(26) Ulrich, C.; Slater, L. Induced polarization measurements on unsaturated, unconsolidated sands. *Geophysics* **2004**, *69*, 762−771.
(27) Pelton, W. H.; Sill, W. R.; Smith, B. D. Interpretation of complex resistivity and dielectric data. Part 1. *Geophys. Trans.* **1978**, *29*, 297−330.
(28) Dias, C. Developments in a model to describe low-frequency electrical polarization in rocks. *Geophysics* **2000**, *65*, 437−451.
(29) Jones, D. P. Master's Thesis, Department of geophysics; Colorado School of Mines, 2002; Vol. Master, p 403.
(30) Lesmes, D. P.; Frye, K. M. Influence of pore fluid chemistry on the complex conductivity and induced polarization responses of Berea sandstone. *J. Geophys. Res., Solid Earth* **2001**, *106*, 4079−4090.
(31) Kemna, A. *Tomographic inversion of complex resistivity—theory and application;* Der Andere Verlag: Osnabrück, Germany, 2000.
(32) Brunauer, S.; Emmett, P. H.; Teller, E. Adsorption of gases in multimolecular layers. *J. Am. Chem. S.* **1938**, *60*, 309−319.
(33) Legrand, L.; Savoye, S.; Chausse, A.; Messina, R. Study of oxidation products formed on iron in solutions containing bicarbonate/carbonate. *Electrochim. Acta* **2000**, *46*, 111−117.
(34) Gu, B.; Phelps, T. J.; Liang, L.; Dickey, M. J.; Roh, Y.; Kinsall, B. L.; Palumbo, A. V.; Jacobs, G. K. Biogeochemical dynamics in zero-valent iron columns: Implications for permeable reactive barriers. *Environ. Sci. Technol.* **1999**, *33*, 2170−2177.
(35) Simard, S.; Odziemkowski, M.; Irish, D. E.; Brossard, L.; Menard, H. In *191st Meeting of the Electrochemical Society;* Montreal, Quebec, 1997; Vol. 97, pp 279−280.

Received for review October 20, 2005. Revised manuscript received January 20, 2006. Accepted January 23, 2006.

ES0520868